

Magnetosphere of Hot Jupiter HD209458b and transit absorption in lines related to the upper atmosphere

Ildar Shaikhsislamov¹, Maxim Khodachenko², Ilya Miroshnichenko¹, Marina Rumenskikh¹, and Artem Berezutsky¹

¹Institute of Laser Physics SB RAS, Novosibirsk, Russian Federation (ildars@ngs.ru)

²Space Research Institute, Austrian Academy of Sciences, Graz, Austria

ABSTRACT: The signs of an expanding atmosphere of HD209458b have been observed with far-ultraviolet transmission spectroscopy and in the measurements of transit absorption by metastable HeI. These observations are interpreted using the hydrodynamic and Monte-Carlo numerical simulations of various degree of complexity and consistency. At the same time, no attempt has been made to model atmospheric escape of a magnetized HD209458b, to see how the planetary magnetic field might affect the measured transit absorption lines. We present the global 3D MHD self-consistent simulations of the expanding upper atmosphere of HD209458b interacting with the stellar wind, and models the observed HI (Ly α), OI (1306 Å), CII (1337 Å), and HeI (10830 Å) transit absorption features. We find that the planetary dipole magnetic field with the equatorial surface value of $B_p=1$ G profoundly changes the character of atmospheric material outflow and the related absorption. We also investigate the formation of planetary magnetosphere in the stellar wind and show that its size is more determined by the escaping atmosphere flow rather than by the strength of magnetic field. Fitting of the simulation results to observations enables constraining the stellar XUV flux and He abundance at $F_{XUV} \sim 10$ erg cm² s⁻¹ (at 1 a.u.) and He/H \approx 0.02, respectively, as well as setting an upper limit for the dipole magnetic field of $B_p < 0.1$ G on the planetary surface at the equator. This implies that the magnetic dipole moment μ_p of HD209458b should be less than 6% of the Jovian value.

1. INTRODUCTION

Vidal-Madjar et al. (2003) observed the primary transits of HD209458b in Ly α with the STIS spectrograph on board of HST and reported 15% absorption in the high velocity blue wing of the line. The primary transit measurements of HD209458b at far UV wavelengths (with HST/STIS) also revealed the absorption depths of $10 \pm 4.5\%$ in OI ($2p^2$ $2P-2p^2$ $2D$) and $7.5 \pm 3.5\%$ in CII ($2p^4$ $3P-2p^4$ $3S$) resonance lines (*Vidal-Madjar et al. 2004*). *Linsky et al. (2010)* analyzed four additional far UV transit observations by COS/HST spectrograph and confirmed the depth of $7.8 \pm 1.3\%$ in CII line.

A new opportunity to probe the expanding atmospheres of HJs and warm Neptunes is opened by the measurements of the metastable helium 2^3S triplet line at 10830 Å (hereafter HeI(2^3S); *Seager & Sasselov 2000*; *Oklopčić & Hirata 2018*). For HD209458b the transit at 10830 Å was measured by *Alonso-Floriano et al. (2019)* using the ground-based Calar Alto CARMENES instrument. The detected excess absorption at the line center was at the level of $0.91 \pm 0.10\%$ with the width of the line 11 km/s in Doppler shifted velocity units. The 9 σ fidelity level leaves no doubt regarding the presence of HeI in the upper atmosphere of HD209458b, which occupies a region of at least 2-3 planet radii R_p around the planet.

Such an extensive observational material available for the HD209458b, makes this HJ a primary candidate for the application of complex numerical models aimed at interpretation of the measurements and inferring physical parameters and features of the stellar-planetary system, such as the mass loss of the planet, abundances of its upper atmospheric species, the parameters of stellar wind (hereafter SW) flow, and the stellar radiation flux. Such models have been continuously developed over the last decade by different research groups, while increasing in complexity and details of the simulated phenomena.

However, the 1D HD models have difficulties with explanation of the observed absorption depths in OI, CII and SiIII lines for HD209458b at the levels comparable to (or even exceeding) those measured in Ly α line. The only reasonable mechanism to produce the line broadenings comparable to the observations, is related with a global flow of the escaping planetary atmospheric material outside the Roche lobe. To simulate the planetary wind (PW) motion beyond the Roche lobe, at least a 2D HD model is needed.

Planetary intrinsic Magnetic Field (hereafter MF) is another important factor which affects the PW and SW interaction and the related transit absorption features. Theoretical estimates (*Grießmeier et al. 2004, 2005, 2007, Khodachenko et al. 2012*) predict that the tidally locked gas giants should have significantly smaller intrinsic MFs than

those of their Solar System’s analogues. There is also an alternative point of view (Reiners & Christensen, 2010), based on the scaling properties of evolution of the convection-driven dynamos (Christensen & Aubert 2006), which predicts rather high intrinsic MFs of HJs, decreasing during the lifetime of a planet, as well as independence of the magnetic dipole moment μ_P on planet rotation (Reiners & Christensen 2010). Therefore the estimation of planetary intrinsic MF still remains an open issue. It is worth to mention in this respect that the numerical simulation of the MF-sensitive measurable phenomena, such as transit absorption of different spectral lines dependent of the planetary material dynamics affected by the MF, opens a way for indirect probing of the exoplanetary MF by fitting the numerical modelling results to observations. An example of such study is presented in this paper.

The realistic simulation of absorption in the lines of various species in presence of planetary MF requires a 3D multi-fluid MHD code, which self-consistently combines the aeronomy of upper atmosphere and the global dynamics of the SW. In the present work we make a step forward on the way of creation of a global multi-fluid 3D MHD self-consistent model of the interacting PW and SW of a HJ, and simulate with it the transit absorption features of HD209458b in the most of the observed spectral lines, such as HI(Ly α), OI, CII and HeI(2³S), taking into account the influence of a planetary MF. It should be noted, that inclusion into consideration of the HeI(2³S) triplet quantitatively and qualitatively broadens the base for comparison between the observations and simulations.

2 THE NUMERICAL MODEL AND BASIC ISSUES

The global 3D multi-fluid HD model used as a basis in the present work has been already described in our earlier papers, e.g., Shaikhislamov *et al.* (2018b, 2020a,b,c) and Khodachenko *et al.* (2019, 2021). It was developed as an upgrade of the previous 1D (Shaikhislamov *et al.* 2014) and 2D (Khodachenko *et al.* 2015, 2017, Shaikhislamov *et al.* 2016) models. The model code solves numerically the hydrodynamic equations of continuity, momentum, and energy for all species of the simulated multi-component PW and SW plasmas. Among the considered species, the model, used in this paper, includes hydrogen and helium particles (H, H⁺, He, He⁺, He²⁺) as well as the heavier particles, O and C in atomic and up to Z=3 ionization levels. The H, He, C, and O chemistry is governed by photo-ionization, dielectronic recombination, electron impact excitation and

ionization. Photo-ionization results also in the strong heating of the gas by the produced photo-electrons, which drives the hydrodynamic outflow of the planetary upper atmospheric material. The corresponding heating term is derived by integration of the absorption cross-sections of species over the XUV spectrum ($\lambda < 912 \text{ \AA}$), taking into account the attenuation of photons in the atmosphere according to the wavelength-dependent cross-section. As a proxy for the XUV flux, F_{XUV} , of the solar-like star HD209458, we use the solar spectrum. However, for the near-ultraviolet (NUV) ($912 < \lambda < 3000 \text{ \AA}$) and near-infrared (NIR) parts of the stellar radiation flux, F_{NUV} and F_{NIR} , respectively we employ a synthetic stellar spectral energy distribution (SED), computed with the LLmodels stellar atmosphere code (Shulyak *et al.* 2004), specifically for HD209458.

The major novelty of this work consists in the inclusion of planetary MF into the previously developed global multi-fluid HD model and its extension to an MHD one. The elaborated new multi-fluid MHD model self-consistently simulates the expansion and escape of the multi-species exoplanetary upper atmosphere, driven by the stellar radiative heating and gravitational forces, and its interaction with the surrounding SW plasma flow, which is also simulated within the model. The set of MHD equations is solved in a global non-inertial spherical frame, centered at the planet and rotating in phase with its orbital motion, i.e., in a so-called tidally locked frame of reference. The polar-axis, Z, and the planetary magnetic dipole moment, μ_P , are directed perpendicular to the equatorial plane, coplanar to the ecliptic. To keep the number of points in the numerical code tractable for processing, the applied radial mesh is highly non-uniform, with the grid step increasing linearly from the planet surface. This allows resolving of the highly stratified upper atmosphere of the planet, where the grid step is as small as $\Delta r = R_p/400$. The latitudinal mesh also varies, typically from $\Delta\theta = 0.05$ at the equator up to $\Delta\theta = 0.15$ at the polar axis to reduce refining of the azimuthal mesh at the poles. The numerical scheme is fully explicit, with the second order accuracy of the space and time discretization. We calculate the MF induction equation assuming that the divergence of the MF is zero, however we do not clean specially the divergence. At the inner boundary of the computation domain, i.e. at the provisional optical radius of the planet $r = R_p$, we fix the MF flux by fixing the radial component of the magnetic dipole field $B_r = \text{const}$, while the perturbations of the azimuthal and poloidal components of the field obey an open boundary condition $\partial_r (r \cdot \delta B_\perp) = 0$.

For the self-consistent calculations on the scale of the whole star-planet system, we incorporate in the same code the simulation of the SW plasma flow, parametrized with the total stellar mass loss rate, M'_{sw} , coronal temperature, T_{cor} , and terminal SW speed, $V_{sw,\infty}$ (see, e.g., in *Khodachenko et al. 2019, Shaikhislamov et al. 2020a*). For these parameters we take the typical solar values.

3 SIMULATION RESULTS

3.1 Absorption at 10830 Å

The main novelty of the present study, besides of the account of possible planetary MF, consists in the calculation of synthetic transit absorption by the HeI(2^3S) atoms and comparing it with the observations. The crucial difference of HD209458b, as compared to other exoplanetary systems we have studied with respect to absorption at HeI(2^3S) 10830 Å line, is that the NUV flux of the host HD209458 star appears to be very strong due to the relatively large stellar size and high temperature of photosphere. Because of that, the main depopulation process of the metastable HeI(2^3S) is the photo-ionization (with a threshold at 2600 Å). This time is sufficiently short to reduce the effect of the radiation pressure on HeI(2^3S) atoms, which otherwise would accelerate them up to extremely high velocities. The HeI(2^3S) atoms are created

mainly by the recombination of He⁺ ions, which in turn are produced by the photoionization of HeI(1^1S) by the high energy XUV radiation at $\lambda < 512$ Å. Therefore, the HeI(2^3S) absorption at 10830 Å depends on the XUV flux F_{XUV} and helium abundance. Both these parameters are in fact poorly constrained. At the same time, the NIR flux, F_{NIR} , and therefore also F_{10830} , provided by the employed synthetic stellar SED, are fixed for the given parameters of the host star, HD209458. So, they cannot be varied in the simulations, whereas the range of possible variation of the NUV flux, F_{NUV} , due to the uncertainty on the stellar parameters can be only within a factor of 2.

Figure 1 shows the excess absorption at the position of metastable HeI(2^3S) triplet at 10830 Å, obtained in the model runs N1, N2, N3, and N4 with different F_{XUV} values. The corresponding He abundance values (see in Table 1) were chosen to fit approximately the measurement data. One can see a relatively good agreement of the simulations with the measurements of *Alonso et al. (2019)* in amplitude and line width. However, the model cannot reproduce the slight (~ 1.5 km/s) blue shift of the absorption maximum and the increased absorption in the blue wing of the line at the Doppler velocities range of $[-20; -10]$ km/s. With a set of trial modelling runs we made sure that even a 5-fold reduction of F_{NUV} cannot help in reproducing these features of the absorption profile. The line core is absorbed very close to the planet, at the

N	F_{XUV} [erg cm ⁻² s ⁻¹], at 1 a.u.	F_{NUV} [erg cm ⁻² s ⁻¹], at 1 a.u.	He/H	M'_p [$\times 10^{10}$ g/s]	A_{HI} %	A_{OI} %	A_{CII} %	A_{HeI} %	B_p [G] / μ_p [μ_J]	M'_{sw} [$\times 10^{10}$ g/s]
1	7.5	$5 \cdot 10^4$	0.05	16.9	8.0	3.7	3.2	0.65	0 / 0	10^2
2	4.0	$5 \cdot 10^4$	0.1	7.4	7.3	3.2	2.7	0.67	0 / 0	10^2
3	15	$5 \cdot 10^4$	0.02	32.4	9.0	6.3	5.9	0.45	0 / 0	10^2
4	10	$3 \cdot 10^4$	0.02	25.8	9.1	6.5	6.1	0.51	0 / 0	10^2
5	4.0	$2.5 \cdot 10^4$	0.02	13.4	12	4.4	3.7	0.28	0 / 0	10^2
6	10	$3 \cdot 10^4$	0.02	11.8	6.7	4.0	3.7	0.48	1 / 0.61	10^2
7	10	$3 \cdot 10^4$	0.02	16.8	7.6	4.3	4.3	0.40	0.5 / 0.3	10^2
8	10	$3 \cdot 10^4$	0.02	20.4	8.6	5.3	5.1	0.41	0.25 / 0.15	10^2
9	10	$3 \cdot 10^4$	0.02	23.1	8.8	6.0	5.7	0.45	0.1 / 0.061	10^2
10	10	$3 \cdot 10^4$	0.02	25.8	9.1	6.5	6.1	0.50	0.025 / 0.015	10^2
11	10	$3 \cdot 10^4$	0.02	15.6	13.5	6.1	5.1	0.89	0 / 0	$2.5 \cdot 10^3$
12	10	$3 \cdot 10^4$	0.02	11.9	7.7	4.4	3.6	0.8.5	1 / 0.61	$2.5 \cdot 10^3$
13	10	$3 \cdot 10^4$	0.02	15.6	15.0	5.6	4.5	0.83	0 / 0	$2.5 \cdot 10^3$ ^{*3}
14	10	$3 \cdot 10^4$	0.02	11.9	6.0	3.8	3.0	0.74	1 / 0.61	$2.5 \cdot 10^3$ ^{*3}
					8.6 ± 2.0 ^{*1}	10.5 ± 4.4 ^{*2}	7.4 ± 4.7 ^{*2}	0.47 ± 0.1		

Table 1. The list of simulation scenarios, with corresponding modeling parameters, and the calculated absorption. Columns from left to right: the number of the model run; the assumed values of stellar XUV and NUV fluxes at 1 a.u. in erg cm⁻² s⁻¹; helium abundance; the calculated mass loss rate of the planet in units of 10^{10} g/s; the calculated total integrated absorption in the lines of HI (Ly α), OI, CII and HeI(2^3S); the assumed equatorial surface value of magnetic field and the corresponding planetary magnetic dipole moment μ_p in units of the Jovian magnetic moment $\mu_J = 1.56 \times 10^{27}$ A m²; the total mass loss rate of the star in units of 10^{10} g/s, used for the simulation of SW.

The integration of absorption over the lines was performed in the following Doppler velocity intervals:

HI (Ly α): ± 200 km/s, excluding ± 50 km/s around the line center;

OI: ± 50 km/s (averaged over the triplet) with the exclusion of ± 6 km/s interval for the transition 1-2 at 1302 Å;

CII: ± 90 km/s (averaged over the triplet) with the exclusion of ± 6 km/s interval for the transition 3/2-1/2 at 1334.5 Å;

HeI: ± 10 km/s around 10833.2 Å;

^{*3} in these model runs a high-speed SW is simulated with velocity 300 km/s at the planet orbit.

The bottom row shows the measured absorption values analyzed in ^{*1} *Ben-Jaffel (2007, 2008)* and ^{*2} *Vidal-Madjar et al. (2004)*

altitudes of $(1-1.5)R_p$, where besides of photoionization, the reaction with H atoms also destroys efficiently the population of metastable HeI(2^3S). Therefore, the acceleration time of HeI(2^3S) atoms by the radiation pressure still remains short (in the regions where it matters). Since the F_{NUV} and F_{XUV} values are not sufficiently constrained and could vary due to the natural fluctuations up to several times, the helium abundance iteratively derived by tuning of the modelling results to the measured HeI(2^3S) absorption at 10830 Å can be constrained only by a factor of ~ 2.5 .

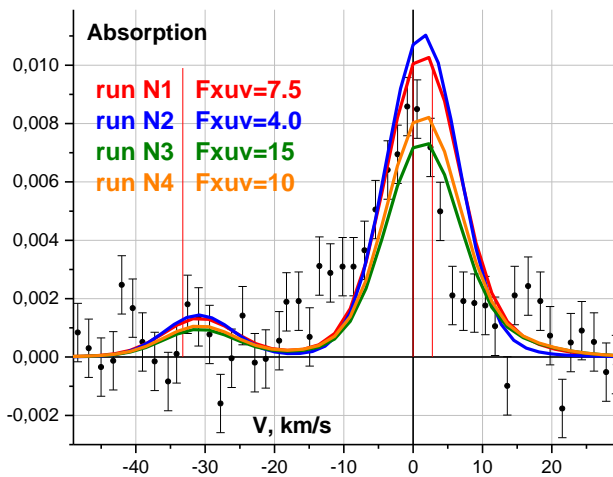


Figure 1. HeI(2^3S) triplet absorption profiles, simulated with different F_{XUV} and He abundances in the model runs N1, N2, N3, N4. Here and further on in similar plots the filled circles with error bars reproduce the measurements from *Alonso et al. (2019)* and red vertical lines indicate the positions of individual lines in the triplet.

3.2 Absorption at HI, OI, CII lines

To constrain further the major model parameters, we calculate the absorption in HI(Ly α) line and the resonant triplets of OI and CII, assuming the solar abundances for oxygen and carbon. As it was found out in our previous paper (*Shaikhislamov et al. 2020a*) and confirmed here, the increasing helium abundance decreases the absorption in all considered lines, because of the decrease of the atmospheric height scale (see, e.g., the model runs N2 and N5 for comparison). On the other hand, the absorption increases with the increasing F_{XUV} because of the faster expansion and escape of the upper atmosphere of the planet. This trend is however reversed, because of the faster ionization of the absorbing elements (see, e.g., the model runs N3, N4, and N5 for comparison). Therefore, confining all the considered absorption profiles within the measurement error margins enables to restrict the ranges for the helium

abundance and XUV flux at $\text{He}/\text{H}=(2\pm 0.25)\cdot 10^{-2}$ and $F_{\text{XUV}}=10\pm 2 \text{ erg cm}^{-2} \text{ s}^{-1}$ (at 1 a.u.), respectively.

The best correspondence with observations is achieved in the model run N4. The worse fit among the considered lines takes place for the OI triplet, which shows relatively small absorption. It is necessary to mention, that in order to fit the depth of the absorption at HeI(2^3S) triplet line addressed in the previous subsection, we took $F_{\text{NUV}}=3\cdot 10^4 \text{ erg cm}^{-2} \text{ s}^{-1}$. The reduced χ^2 for HeI(2^3S) line in the range of Doppler velocities $\pm 20 \text{ km/s}$ in the model run N4 is 3.2. At the same time, simple shifting of the whole absorption profile by -1.5 km/s decreases the reduced χ^2 down to 1.84. Thus, the question of whether the observed small ($\sim 1.5 \text{ km/s}$) blue shift is real remains important.

3.3 Effect of the planetary magnetic field

Imposing a relatively strong planetary dipole MF with a value of $B_p=1 \text{ G}$ at the surface of planet on the equator, which corresponds to the planetary magnetic dipole moment $\mu_p=0.61$ in units of the Jovian magnetic moment, profoundly changes the modeled atmospheric outflow of HD209458b, especially in the vicinity of the planet. This scenario is realized in the model run N6, which differs from the model run N4 just by the inclusion of the planetary MF. The color plot in Figure 2A shows the obtained distribution of the planetary and stellar proton density in the whole simulated domain, whereas Figure 2B presents the structure of the calculated planetary magnetosphere, viewed in the plane orthogonal to the ecliptic. As found out in our previous 2D simulations (*Khodachenko et al. 2015*) and predicted in earlier semi-analytic considerations (*Khodachenko et al. 2012*), the outflowing PW material stretches and opens the magnetic dipole field lines and forms an equatorial current layer, so-called magnetodisk. The shape and structure of the formed magnetodisk-type electric current layer are shown in Figure 3. Although it surrounds the planet in the equatorial plane, it is not uniform.

The comparison of simulation results, obtained for the magnetized and non-magnetized planet, i.e. with $B_p=1 \text{ G}$ and $B_p=0 \text{ G}$ in the model runs N6 and N4, respectively, reveals first of all, the two times decrease of the planetary mass loss rate due to decreasing velocity and density of the escaping PW. Second, the MF causes significant reduction in the lines' absorption. To understand why this happens we provide in Figure 4 the density profiles of the corresponding absorbing elements. As can be seen, while the escaping PW material temperature remains almost the same, its velocity in the presence of MF is significantly reduced in a relatively extended ($\approx 2.5R_p$) region around the

planet. This region corresponds to a so called ‘dead’ zone, where the planetary plasma escape is suppressed by the MF. Beyond the ‘dead’ zone, velocity sharply increases and quickly reaches the values typical for the non-magnetized case. Inside the thin magnetodisk, which has a thickness of about $\pm 0.5 R_p$, the MF is reduced, but it increases sharply in the lobes, whereas the plasma pressure behaves in the opposite way.

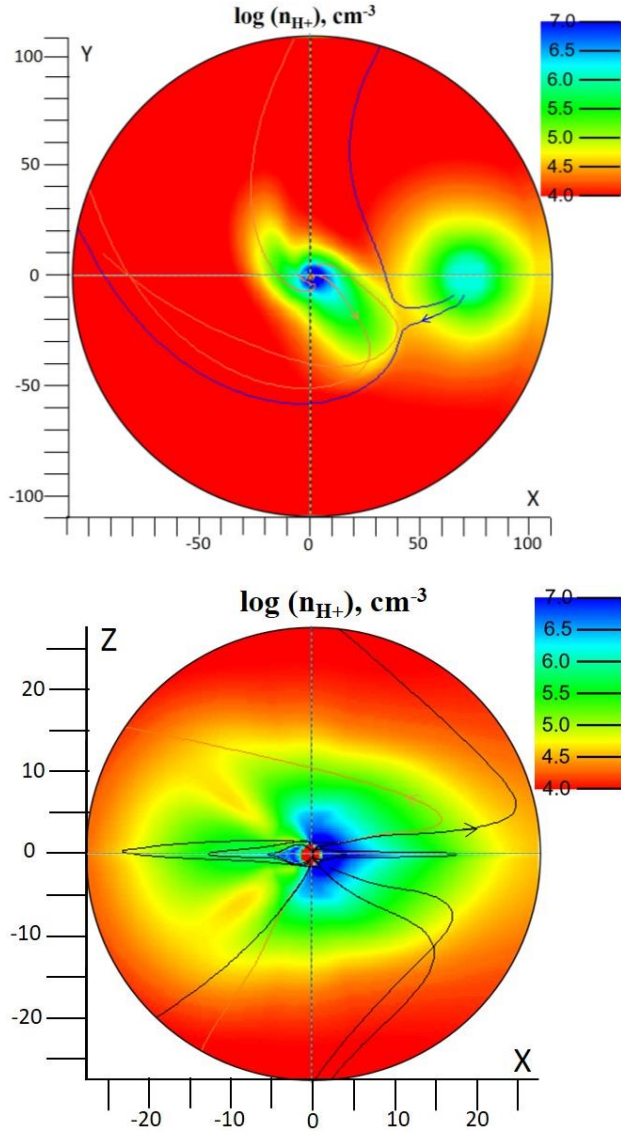


Figure 2. *Upper Panel:* proton density distribution in the orbital plane of the simulated domain, calculated in the model run N6, i.e., with $B_p=1$ G and other parameters the same as in the model run N4. The planet is at the center of the coordinate system (0,0) and moves anticlockwise relative the star located at (70,0). *Lower Panel:* proton density distribution and MF lines (black) in the meridional plane around the planet. Proton fluid streamlines originated from the planet (orange) and from the star (blue) are shown in both panels. The axes, here and further on in the spatial distribution plots, are scaled in planetary radii R_p .

The significantly reduced escape velocity in the case of a magnetized planet leads to a longer

exposure of atoms to XUV radiation and consequently, to the stronger photo-ionization. Figure 4A shows the ratio of magnetic pressure at the edge of magnetodisk (at $Z=0.5 R_p$) to the plasma pressure at $Z=0$. They appear in a close balance (if corrected for the lines curvature). This balance and the structure of magnetodisk have been addressed in *Khodachenko et al. (2015)*. It is worth to mention, that despite the strong influence of MF on the motion of escaping planetary material close to the planet, it does not influence the interaction between the PW and SW in a more distant region, because for the considered SW intensity the ionopause is located far beyond the magnetically dominated region.

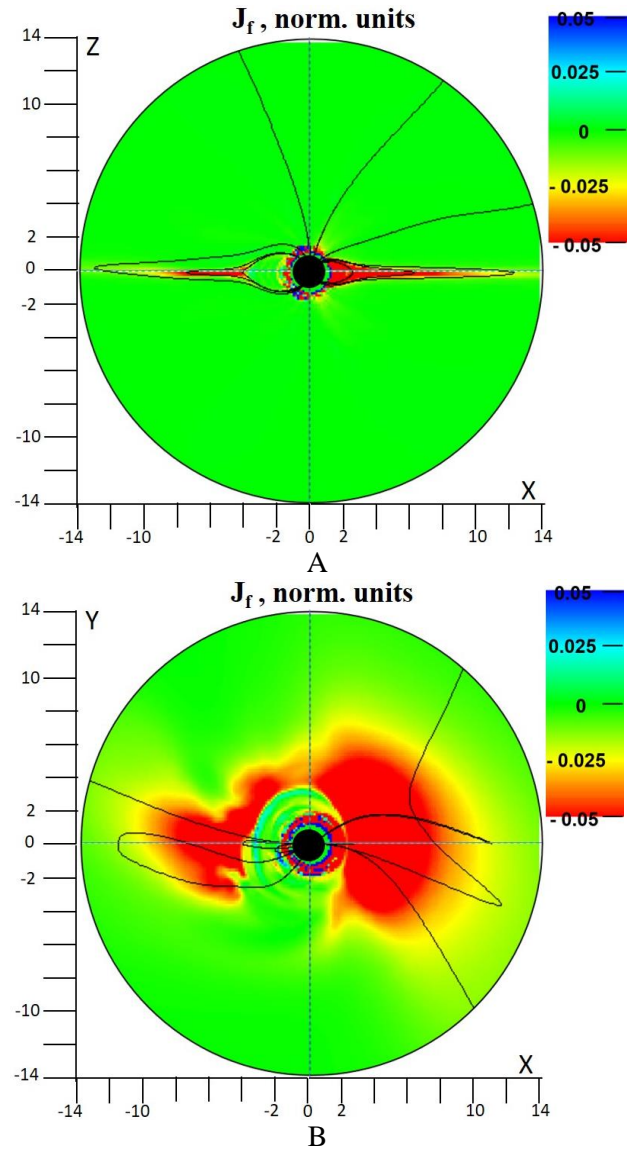


Figure 3. Distribution of the azimuthal component of electric current in the meridional (*Panel A*) and orbital (*Panel B*) planes, obtained in the model run N6. MF lines are shown in black.

Therefore, the reduced densities of HI, OI, and CII, clearly seen in panel B of Figure 4, would result in

the decrease of absorption. The density profiles of HI, OI, and CII in Figure 4B are given along the observer's line of sight (LOS) at the altitude $r=2R_p$, i.e., beyond the photometric radius of the planet. One can see that when $B_p=1$ G, the densities of HI, OI, and CII are significantly reduced, especially on the night-side, behind the planet, where the influence of MF on the outflowing PW velocity, as compared to the thermal pressure, is the strongest. Detailed illustration of how the MF affects the absorption is given in Figure 5, where the spectral absorption profiles at the OI 1305 Å and CII 1336 Å lines are shown.

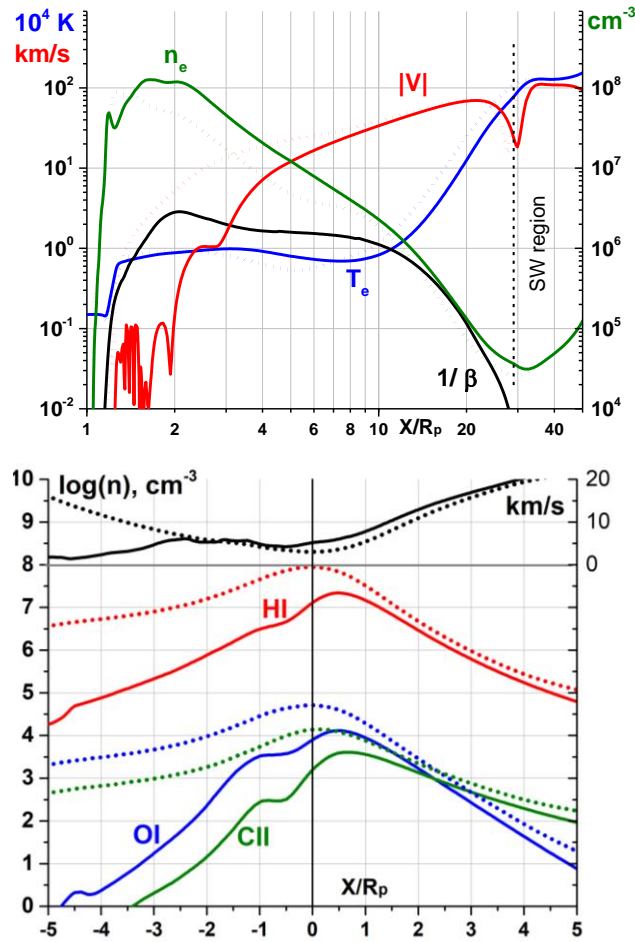


Figure 4. Distribution of major physical quantities along the observer's line of sight (X -axis), calculated for the magnetized ($B_p=1$ G, solid lines) and non-magnetized planet ($B_p=0$ G, dotted lines) in the model runs N6 and N4, respectively. *Upper Panel:* proton velocity (red, left axis); electron temperature (blue, left axis); electron density (olive, right axis); ratio of magnetic pressure at $Z=0.5 R_p$ (the edge of magnetodisk) to plasma pressure at $Z=0$, i.e. analog of the inversed plasma-beta (black, right axis) along the planet-star line (at the level $Z=Y=0$). The vertical dashed line indicates the position of boundary between the planetary and SW plasmas (i.e., ionopause). *Lower Panel:* log of density of hydrogen atoms (red, left axis); neutral oxygen (blue, left axis); ionized carbon (olive, left axis); and flow velocity (black, right axis) at the level of $Z=Y=1.4 R_p$.

Comparison of the spectral absorption profiles in Figure 5 reveals that the planetary MF results in narrowing of the absorption profile in the blue wing, due to the decreased velocity of the escaping PW, especially on the planet night-side; and the decreased absorption maxima in the line centers, due to the lower densities of absorbing elements around the planet (see, e.g., in Figure 4). The contribution of velocity V of the escaping planetary atmospheric material to the calculated absorption is demonstrated in Figure 5, which shows also the absorption profiles obtained with an 'ad hoc' prescribed zero velocity of PW. We found that for the magnetized planet the full integrated absorption values in the cases with $V \neq 0$ and $V=0$ are rather close. This confirms that the natural line broadening is a dominating mechanism of absorption in the magnetized HD209458b.

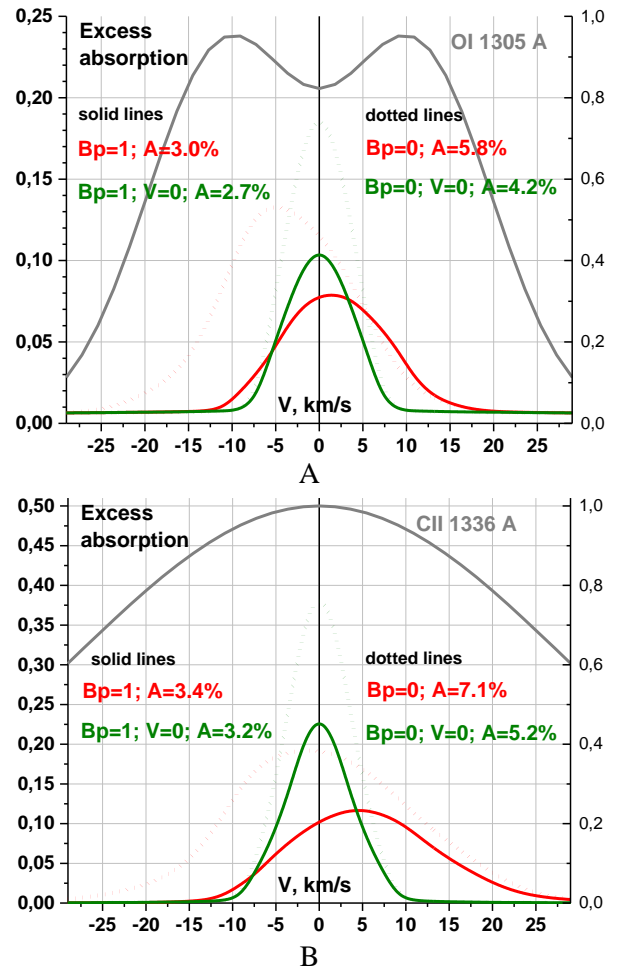


Figure 5. Absorption profiles at the OI 1305 Å (*Panel A*) and CII 1336 Å (*Panel B*) lines over Doppler-shifted velocity, calculated in the model runs N4 and N6. Dotted and solid lines correspond to the non-magnetized ($B_p=0$, model run N4) and magnetized ($B_p=1$ G, model run N6) cases, respectively; gray lines show the stellar emission line shapes used to calculate the absorption. Red lines show the full absorption in particular lines by the considered elements (to be compared with observations); olive lines show the full absorption calculated with the

velocity of species artificially set to zero. The full integrated absorption values in each case are given in the legend.

Without MF the velocity of escaping PW contributes about $1.5 \pm 2\%$ to the absorption. This is due to the Doppler resonant line broadening, discussed in *Khodachenko et al. (2017)*. At the same time, the distribution of the absorbing particles across the LOS in front of the stellar disk reveals that in the case of magnetized planet they obscure the area of $\sim 3R_p$ around the planet, while in the case of non-magnetized planet this area extends up to $5R_p$.

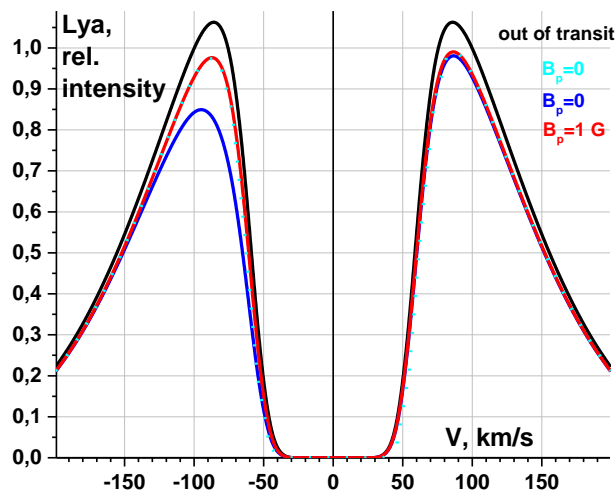


Figure 6. Simulated $\text{Ly}\alpha$ in-transit profiles versus the out-of-transit profile. *Cyan dotted line*: non-magnetized planet in moderate SW (model run N4); *blue line*: non-magnetized planet in strong SW (model run N11); *red line*: magnetized planet ($B_p=1$ G) in strong SW (model run N12); *black line*: the out-of-transit $\text{Ly}\alpha$ profile based on measurements by *Vidal-Majar et al. (2003)*.

The calculation of absorption in the model runs N6-N10, for the decreasing values of B_p , from 1G down to 0.025G, with all other parameters of the system kept the same, reveals the gradual increase of the planetary mass loss and the absorption at all the considered lines, except of the $\text{HeI}(2^3\text{S})$ line. By this, even for $B_p=0.1$ G its effect is still persistent, while being smaller than in the case of $B_p=1$ G. In particular, for $B_p=0.1$ G, the absorption at the lines of OI and CII appears 0.5% less than that in the non-magnetized case. Altogether, the closest match to the measurements in all considered lines is achieved in the model runs N9 and N10, which correspond to $B_p=(0.1-0.025)$ G, or the planetary magnetic dipole $\mu_p < 0.1$ in units of the Jovian value. The revealed stronger sensitivity of the absorptions at OI and CII lines to the value of MF, as compared with $\text{HI}(\text{Ly}\alpha)$ absorption, is due to their stronger relation with the moving PW controlled by the MF,

whereas $\text{Ly}\alpha$ absorption on HD209458b takes place in the relatively close to the planet regions within the Roche lobe with an insignificant material motion.

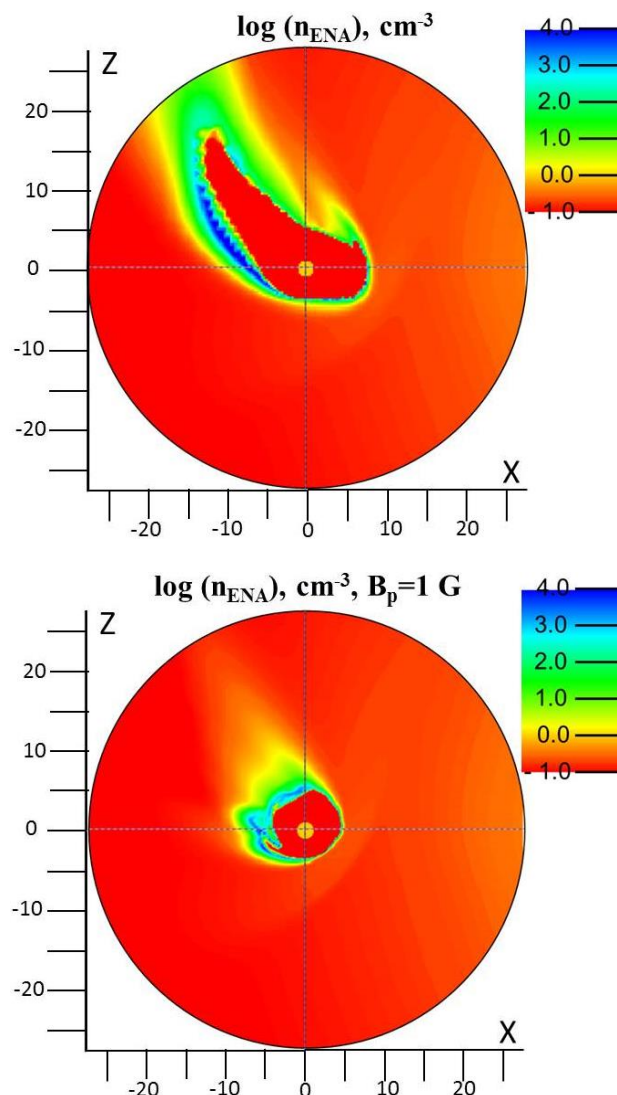


Figure 7. Distribution of ENAs in the orbital plane simulated under the conditions of strong SW in the cases of non-magnetized (*Upper Panel*, model run N11) and magnetized (*Lower Panel*, model run N12) planet.

3.4 Magnetosphere under conditions of a strong SW

Khodachenko et al. (2017) and *Shaikhislamov et al. (2020a)* have shown that a moderate SW does not influence the absorption at the considered lines, whereas the tenfold increased flux of the SW significantly increases the absorption in the blue wing of the $\text{Ly}\alpha$. The latter happens due to the generation of significant amount of ENAs in the PW-SW interaction region. In this subsection we examine how planetary MF affects this scenario. First, in the model run N11 we simulated the case

of a strong SW by taking the increased total stellar mass loss rate of $M'_{sw}=2.5\times 10^{13}$ g/s, with the increased up to $n_{sw}=10^5$ cm⁻³ density at the planet orbit, while keeping the same as in the previously considered moderate SW cases velocity, $V_{sw}=220$ km/s and temperature $T_{sw}=8.5\cdot 10^5$ K. The planetary MF was taken to be zero in this model run. Figure 6 shows the Ly α absorption profile which demonstrates under the conditions of the strong SW the absorption in the blue wing with average value of 19% in the range [-150; -50] km/s, which is much deeper than that in the case of a moderate SW. The enhanced absorption in the blue wing is also apparent for the OI and CII lines, though the total integrated absorption value is smaller.

It is worth to note, that for the magnetized planet, the Ly α absorption in the blue wing under the conditions of strong SW becomes practically the same as that in the case of a the non-magnetized planet and moderate SW (see in Figure 6). This is because the amount of ENAs in the magnetized case is suppressed by the MF, affecting the planetary and stellar plasma flows. It is demonstrated in Figure 7, which shows that in the case of the magnetized planet the population of ENAs becomes strongly depleted in the tail region. Altogether, the most of the absorption in the case of magnetized planet and strong SW, like in the case of non-magnetized planet and moderate SW, is due to the natural line broadening mechanism, and it is provided by the atomic hydrogen, confined within the magnetosphere and Roche lobe. This results in the symmetric Ly α absorption profiles obtained in the model runs N4 and N12 (Figure 6).

To study formation of the planetary magnetospheric obstacle and the role of the planetary MF, we consider further the case of a strong SW, but increase its velocity at the planet orbit up to 300 km/s, while keeping the total stellar mass loss rate, $M'_{sw}=2.5\times 10^{13}$ g/s, the same as in the model runs N11 and N12. This fast SW pushes the magnetopause closer to the planet and results in a similar structure of the magnetosphere as that known for the magnetized Solar System planets. The generated magnetospheric current system has the typical components, such as the dipolar MF dominated region around the planet, the magnetopause current sheet at the front of magnetosphere and the return current at high latitudes, as well as the tail current sheet, as seen in Figure 8A. However, the proton density distributions in Figure 8B show that the size of the PW dominated region around the planet in the case of $B_p=1$ G is practically the same as in the non-magnetized case.

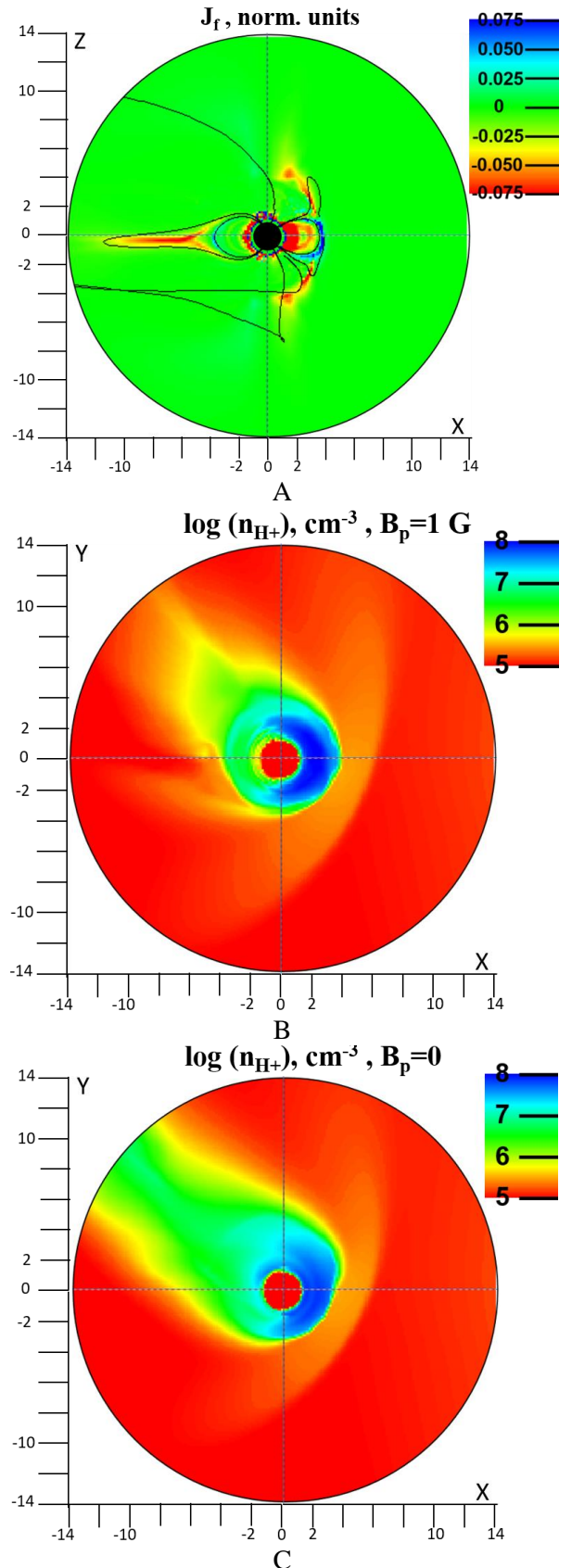


Figure 8. Magnetosphere structure of HD209458b and proton density distribution under the conditions of strong SW simulated in the model run N14. *Panel A:* Distribution of azimuthal current and MF lines in the meridional plane. *Panels B and C:* Proton density distribution in the orbital plane (*Panel B*) as compared to that in the case of non-magnetized planet (*Panel C*, model run N13).

Therefore, we see that, even for a relatively high planetary MF, the modelled escaping PW of HD209458b is strong enough to dominate in the total pressure balance and to compete with the magnetic pressure at the distances of $(3\div 4)R_p$.

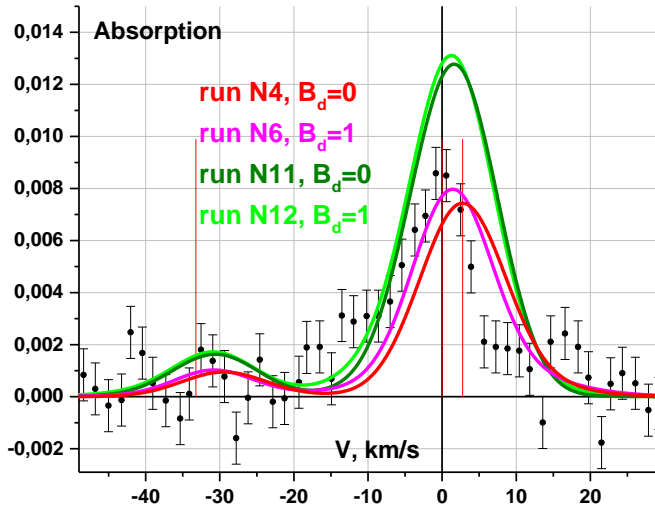


Figure 9. HeI(2^3S) triplet absorption profiles, simulated with the moderate (model runs N4, N6) and strong (model runs N11, N12) SW in the cases of magnetized (model runs N6, N12) and non-magnetized (model runs N4, N11) planet.

Finally, we show in Figure 9 how the planetary MF and intensity of SW might affect the HeI(2^3S) triplet absorption profiles. In particular, the overall effect of MF for $B_p=1$ G is rather small, though the profiles shift slightly towards the blue range. For the strong SW the absorption depth becomes $1.5\div 2$ times higher. This is the consequence of a more compact magnetosphere and/or ionosphere compressed by the SW. At the same time, the blue shift of the HeI(2^3S) absorption profile under the conditions of moderate SW and magnetized planet (the model run N6) provides better correspondence with the measurements in the blue part of the line as compared to the non-magnetized case (the model run N4), while in the red part the simulated absorption level is still higher than the observed one. At the same time, the simulated absorption in other considered lines still remains different from the measured values (see in Table 1).

4 DISCUSSION AND CONCLUSIONS

Using the global 3D multi-fluid HD and MHD models we simulated the measured HD209458b transit absorption depths at the far UV lines, and at the NIR line (10830 Å) of HeI(2^3S) triplet. As continuation of our previous studies of HD209458b,

the inclusion of the HeI(2^3S) line into consideration and the comparison with corresponding measurements allows to constrain the helium abundance by $\text{He}/\text{H} \sim 0.02$, and the stellar XUV flux at 1 a.u. by $F_{\text{XUV}} \sim 10 \text{ erg cm}^2 \text{ s}^{-1}$. While the simulated peak and half-width of the HeI(2^3S) absorption profile fit the observations reasonably well, there is a net blue shift of $\sim 1.5 \text{ km/s}$ which the model cannot reproduce with the assumed variability of the parameters, affecting the HeI(2^3S) line. At the same time, to verify the applied constrains on the helium abundance and the XUV flux values, and to exclude the effects of the stellar short-periodic variability, more measurements are needed. For example, two available measurements at 10830 Å for the HD189733b show a factor of 1.5 difference, which could be related with the varying stellar radiation.

For the first time, we study in this paper the influence of the planetary dipole MF on the absorption in the most of spectral lines simultaneously, for which the measurements have been made. Our MHD simulations show that the planetary magnetic dipole moment $\mu_p=0.61 \cdot \mu_J$, profoundly changes the character of the escaping PW flow and the related absorption. The total mass loss rate in this case is reduced by 2 times, as compared to the non-magnetized planet. All the basic phenomena related to the influence of the planetary dipole MF on the structure of the escaping PW, and revealed in the 2D MHD modeling of the magnetized analog of HD209458b (Khodachenko *et al.* 2015), were also reproduced in the present 3D MHD simulations. In particular we see the formation of the ‘dead’- and ‘wind’- zones around the planet with their different character of plasma motion. The 3D MHD modeling also confirmed the result of previous 2D simulations that the escaping PW forms a thin magnetodisk in the equatorial region around the planet. The significantly reduced velocity of PW at the low altitudes around the planet, and especially at the night side, results in the stronger photo-ionization of species and significantly lower densities of the corresponding absorbing elements. Altogether, these reduced velocities and lower densities result in significant decrease of the absorption at Ly α (HI), OI, and CII lines, though the absorption at HeI(2^3S) line remains nearly the same.

As it was shown in our previous papers, the dense and fast SW interacting with the escaping upper atmosphere of HD209458b, generates sufficient amount of ENAs to produce significant absorption in the high-velocity blue wing of the Ly α line. However, according to the reported here 3D MHD modeling, the planetary magnetic dipole moment of $0.61\mu_J$ with the equatorial MF surface

value $B_p=1$ G prevents the formation of ENAs, especially at the night side. This effect opens a possibility to constrain the range of planetary MF values for the evaporating hot Jupiters and warm Neptunes subject to strong enough SW. As an example of such cases, may be Pi Men C, which reveals rather low Ly α absorption (*García Muñoz et al. 2020, Shaikhislamov et al. 2020b*), despite of qualitative similarity to other warm Neptunes, e.g., GJ436b and GJ3470b, where significant blue shifted Ly α absorption generated by ENAs was measured (*Ehrenreich et al. 2015, Lavie et al. 2017, Bourrier et al. 2018*) and simulated (*Khodachenko et al. 2019, Shaikhislamov et al. 2020c*). As to the absorption at the HeI(2³S) line, the strong SW also results in its increase, though the influence of MF in this case is negligible.

The simulation results presented in this paper indicate that the magnetic dipole moment μ_p of HD209458b should be at least an order of magnitude less than that of the Jupiter. This conclusion agrees with the previous estimates, based on more simplified models (e.g., *Kislyakova et al. 2014*) and less observational data (only Ly α absorption was considered). The application of 3D MHD models, like e.g., that presented here, which self-consistently simulate the escape of upper atmospheres of hot exoplanets and the related transits at several spectral lines available for measurement and sensitive to the PW dynamics affected by the MF, opens the way for probing and quantifying exoplanetary MFs by fitting the modelling results to observations. This altogether will shed more light on the nature of exoplanetary magnetism and related magnetospheric phenomena.

This work was supported by grant № 18-12-00080 of the Russian Science Foundation and grant № 075-15-2020-780 of the Russian Ministry of Education and Science.

REFERENCES

- Allart, R., Bourrier, V., Lovis, C., et al. 2019, A&A, 623, id.A58.
- Alonso-Floriano, F. J., Snellen, I. A. G., Czesla, S., et al. 2019, A&A, 629, id.A110
- Arakcheev, A. S., Zhilkin, A. G., Kaigorodov, P. V., et al. 2017, Astron.Reports, 61(11), 932-941
- Ben-Jaffel, L. 2007, ApJL, 671, L61
- Ben-Jaffel, L. 2008, ApJ, 688, 1352
- Ben-Jaffel, L., Sona Hosseini, S. 2010, ApJ, 709, 1284
- Bourrier, V., Lecavelier des Etangs, A., 2013, A&A, 557, id.A124
- Bourrier, V., Des Etangs, A. L., Ehrenreich, D., et al. 2018, A&A, 620, A147
- Christensen, U. R., Aubert, J. 2006, Geophys. J. Int., 166, 97
- Cubillos, P.E., Fossati, L., Koskinen, T., et al. 2020, ApJ, 159:111
- Daley-Yates, S., Stevens, I. R. 2018, MNRAS, 479, 1194-1209
- Daley-Yates, S., & Stevens, I. R. 2019, MNRAS, 483, 2600-2614
- Debrecht, A., Carroll-Nellenback, J., Frank, A., et al. 2020, MNRAS, 493, 292
- Ehrenreich, D., Bourrier, V., Wheatley, P. J., et al. 2015, Natur, 522, 459
- Erkaev, N. V., Odert, P., Lammer, H., et al. 2017, MNRAS, 470, 4330
- García Muñoz, A. 2007, Planet. Space Sci., 55, 1426
- García Muñoz, A., Youngblood, A., Fossati, L., et al. 2020, ApJ, 888, L21
- Grießmeier, J.-M., Stadelmann, A., Penz, T., et al. 2004, A&A, 425, 753
- Grießmeier, J.-M., Stadelmann, A., Motschmann, U., et al. 2005, Astrobiology, 5, 587
- Grießmeier, J.-M., Preusse, S., Khodachenko, M. L., et al. 2007, Planet. Space Sci., 55, 618
- Guo, J. H. 2011, ApJ, 733(2), 98
- Khodachenko M. L., Alexeev I. I., Belenkaya E., et al. 2012, ApJ., 744, 70-86
- Khodachenko, M.L., Shaikhislamov, I.F., Lammer, H., et al. 2015, ApJ, 813:50.
- Khodachenko, M.L., Shaikhislamov, I.F., Lammer, H., et al. 2017, ApJ, 847:126
- Khodachenko, M. L., Shaikhislamov, I. F., Lammer, H., et al. 2019, ApJ, 885:67
- Khodachenko, M. L., Shaikhislamov, I. F., Fossati, L., et al. 2021, MNRAS: Lett., slab015
- Kislyakova, G. K., Holmström, M., Lammer, H., et al. 2014, Science, 346, 981
- Koskinen, T. T., Yelle, R. V., Lavvas, P., et al. 2010, ApJ, 723, 116
- Koskinen, T. T., Harris, M. J., Yelle, R. V., et al. 2013, Icarus, 226, 1678
- Lavie, B., Ehrenreich, D., Bourrier, V., et al. 2017, A&A, 605, L7
- Lammer, H., Selsis, F., Ribas, I., et al. 2003, ApJL, 598, L121
- Lampón, M., López-Puertas, M., Lara, L. M., et al. 2020, A&A, 636, A13
- Lecavelier des Etangs, A., Vidal-Madjar, A., McConnell, J. C., et al. 2004, A&A, 418, L1
- Lecavelier des Etangs, A., Vidal-Madjar, A., Desert, J.-M. 2008, Nature, 456, E1
- Linsky, J. L., Yang, H., France, K., et al. 2010, ApJ, 717, 1291
- Matsakos, T., Uribe, A., Königl, A. 2015, A&A, 578, A6
- Murray-Clay, R. A., Chiang, E. I., Murray, N. 2009, ApJ, 693(1), 23
- Oklopčić, A., Hirata, C.M. 2018, ApJ Lett., 855, L11
- Oklopčić A., Silva M., Montero-Camacho, P., et al. 2020, ApJ, 890:88
- Parker, E. N. 1958, ApJ, 128, 664
- Penz, T., Erkaev, N. V., Kulikov, Y. N., et al. 2008, Planet. & Space Sci., 56(9), 1260-1272
- Reiners, A., Christensen, U. R. 2010, A&A, 522, A13
- Salz, M., Czesla, S., Schneider, P. C., & Schmitt, J. H. M. M. 2016, A&A, 586, A75
- Seager, S., Sasselov, D. D. 2000, ApJ, 537, 916
- Shaikhislamov, I. F., Khodachenko, M. L., Sasunov, Yu. L., et al. 2014, ApJ, 795:132
- Shaikhislamov, I.F., Khodachenko, M.L., Lammer, H., et al. 2016, ApJ, 832:173
- Shaikhislamov, I. F., Khodachenko, M. L., Lammer, H., et al. 2018a, ApJ, 866:47
- Shaikhislamov, I.F., Khodachenko, M.L., Lammer, H., et al. 2018b, MNRAS, 481, 5315–5323
- Shaikhislamov, I.F., Khodachenko, M.L., Lammer, H., et al. 2020a, MNRAS, 491, 3435–3447
- Shaikhislamov, I. F., Fossati, L., Khodachenko, M. L., et al. 2020b A&A, 639, A109

Shaikhislamov, I. F., Khodachenko, M. L., Lammer, H., et al. 2020c, MNRAS, 2020, 500(1), 1404-1413

Shulyak, D., Tsymbal, V., Ryabchikova, T., et al. 2004, A&A, 428, 993-1000.

Trammell, G. B., Arras, P., & Li, Z.-Y. 2011, ApJ, 728:152

Trammell, G. B., Li, Z. Y., & Arras, P. 2014, ApJ, 788:161

Tripathi, A., Kratter, K. M., Murray-Clay, R. A., et al. 2015, ApJ, 808, 173

Vidal-Madjar, A., Lecavelier des Etangs, A., Désert, J.-M., et al. 2003, Nature, 422, 143

Vidal-Madjar, A., Désert, J., Lecavelier des Etangs, A., et al. 2004, ApJL, 604, L69

Vidal-Madjar, A., Lecavelier des Etangs, A., Désert, J.-M., et al. 2008, ApJ, 676, 157

Vidal-Madjar, A., Huitson, C. M., Bourrier, V., et al. 2013, A&A, 560, A54

Wang, L., Dai, F. 2018, ApJ, 860:175

Yelle, R. V. 2004, Icarus, 170, 167

Zhilkin, A. G., Bisikalo, D. V. 2019, Astron.Reports, 63(7), 550-564

Zhilkin, A. G., Bisikalo, D. V., Kaygorodov, P. V. 2020, Astron.Reports, 64(2), 159-167